

# Microwave Biomedical Imaging Using the Multiplicative Regularized Gauss–Newton Inversion

Puyan Mojabi and Joe LoVetri, *Senior Member, IEEE*

**Abstract**—The weighted  $L_2$ -norm total variation multiplicative regularized Gauss–Newton inversion method, recently developed for inversion of low-frequency deep electromagnetic geophysical measurements, is used for microwave biomedical imaging. This inversion algorithm automatically adjusts the regularization weight and provides edge-preserving characteristics. The accuracy of this method is demonstrated by inverting experimental data of a human forearm and synthetic data taken from brain and breast models, both assuming two-dimensional (2D) transverse magnetic illumination.

**Index Terms**—Biomedical imaging, Gauss–Newton method, inverse problems, microwave imaging (MWI), regularization.

## I. INTRODUCTION

**I**N MICROWAVE IMAGING (MWI), one tries to infer the dielectric profile of an object of interest (OI) using microwave scattering measurements collected outside the OI. There are several important potential biomedical applications for MWI, such as breast cancer imaging [1] and brain imaging [2].

The inverse problem associated with microwave imaging is nonlinear and ill-posed. The nonlinearity of the problem is usually handled by optimizing an appropriate cost-functional using various iterative techniques, and the ill-posedness is usually treated by employing different regularization techniques. Two iterative techniques, the Gauss–Newton inversion (GNI) and the contrast source inversion (CSI) methods, have seen extensive use in the literature for microwave biomedical imaging (e.g., see [1]–[6]). As far as the regularization of the problem is concerned, the weighted  $L_2$ -norm total variation multiplicative regularization (MR) in conjunction with the CSI method [5], known as the MR-CSI method, has been one of the most successful techniques to date. The two main advantages of this regularization are: 1) its edge-preserving characteristic, and 2) providing adaptive regularization where the weight of the regularization is *automatically* adjusted during the optimization by the algorithm itself. On the other hand, most proposed regularization techniques that have been used with the GNI method do not have the edge-preserving characteristic and require *ad hoc* techniques for determining the regularization

weight. Recently, this specific multiplicative regularization has been used with the GNI method to invert low-frequency (from frequencies below 1 to a few hundred Hz) cross-well and controlled-source electromagnetic measurements to reconstruct the conductivity profile in geophysical applications [7], [8].

In this letter, we use this recently formulated multiplicative regularized Gauss–Newton inversion (MR-GNI) method for microwave biomedical imaging assuming the two-dimensional (2D) transverse magnetic (TM) illumination. The data sets against which the MR-GNI is tested include measurement data for a human forearm provided by the Universitat Politècnica de Catalunya (UPC), Barcelona, Spain, [9] and synthetic data taken from brain and breast models.

## II. PROBLEM STATEMENT

Consider a bounded imaging domain  $\mathcal{D} \subset \mathbb{R}^2$  and a measurement domain  $\mathcal{S} \subset \mathbb{R}^2$  outside  $\mathcal{D}$ . Let  $\mathbf{p}$  and  $\mathbf{q}$  denote position vectors in  $\mathbb{R}^2$ , and assume  $\mathbf{p} \in \mathcal{S}$  and  $\mathbf{q} \in \mathcal{D}$ . The imaging domain is immersed in a known background having relative permittivity  $\epsilon_b$ , which contains a nonmagnetic OI with unknown complex relative permittivity  $\epsilon_r(\mathbf{q})$ . The electric contrast function, defined as  $\chi(\mathbf{q}) = (\epsilon_r(\mathbf{q}) - \epsilon_b)/\epsilon_b$ , is to be found using the measured electric field on  $\mathcal{S}$ .

The OI is illuminated by some known incident electric field  $E^{\text{inc}}$ , and the measured scattered field on  $\mathcal{S}$  is then used to reconstruct the OI. Denoting  $E^{\text{meas}}(\mathbf{p})$  as the measured scattered field on  $\mathcal{S}$  and  $E^{\text{scat}}(\mathbf{p}, \chi)$  as the simulated scattered field on  $\mathcal{S}$  due to a predicted contrast  $\chi$ , the inverse problem may be formulated as the minimization over  $\chi$  of the following cost-functional:

$$\mathcal{F}^{\mathcal{L}\mathcal{S}}(\chi) = \frac{1}{\|E^{\text{meas}}(\mathbf{p})\|_{\mathcal{S}}^2} \|E^{\text{scat}}(\mathbf{p}, \chi) - E^{\text{meas}}(\mathbf{p})\|_{\mathcal{S}}^2 \quad (1)$$

where  $\|\cdot\|_{\mathcal{S}}$  denotes the  $L_2$ -norm on  $\mathcal{S}$ . For the 2D TM case, the predicted scattered field  $E^{\text{scat}}(\mathbf{p}, \chi)$  can be found as

$$E^{\text{scat}}(\mathbf{p}, \chi) = k_b^2 \int_{\mathcal{D}} g(\mathbf{p}, \mathbf{q}) E(\mathbf{q}) \chi(\mathbf{q}) d\mathbf{q} \quad (2)$$

where  $g(\mathbf{p}, \mathbf{q})$  is the known 2D scalar Green's function for the background medium and  $k_b$  is the wavenumber of the background medium. Note that  $E^{\text{scat}}(\mathbf{p}, \chi)$  is a nonlinear function with respect to  $\chi(\mathbf{q})$  because the total field,  $E(\mathbf{q})$ , is a function of  $\chi(\mathbf{q})$  which may be expressed as

$$E(\mathbf{q}) = E^{\text{inc}}(\mathbf{q}) + k_b^2 \int_{\mathcal{D}} g(\mathbf{q}, \mathbf{q}') E(\mathbf{q}') \chi(\mathbf{q}') d\mathbf{q}'. \quad (3)$$

Manuscript received April 28, 2009. First published May 26, 2009; current version published July 09, 2009.

The authors are with the Department of Electrical and Computer Engineering, University of Manitoba, Winnipeg, MB R3T 5V6, Canada (e-mail: pmojabi@ee.umanitoba.ca).

Color versions of one or more of the figures in this letter are available online at <http://ieeexplore.ieee.org>.

Digital Object Identifier 10.1109/LAWP.2009.2023602

The cost-functional  $\mathcal{F}^{\mathcal{L}\mathcal{S}}(\chi)$  is therefore also nonlinear with respect to the unknown contrast. In addition, it is well known that this cost-functional is ill-posed and requires regularization. At the  $(n+1)$ th iteration of the inversion algorithm, we form the multiplicative regularized cost-functional  $\mathcal{F}_{n+1}(\chi)$  as [7]

$$\mathcal{F}_{n+1}(\chi) = \mathcal{F}^{\mathcal{L}\mathcal{S}}(\chi)\mathcal{F}_{n+1}^{\text{MR}}(\chi). \quad (4)$$

The weighted  $L_2$ -norm total variation multiplicative regularizer  $\mathcal{F}_{n+1}^{\text{MR}}(\cdot)$  is given as

$$\mathcal{F}_{n+1}^{\text{MR}}(\chi) = \frac{1}{A} \int_{\mathcal{D}} \frac{|\nabla\chi(\mathbf{q})|^2 + \delta_n^2}{|\nabla\chi_n(\mathbf{q})|^2 + \delta_n^2} d\mathbf{q} \quad (5)$$

where  $\nabla$  denotes the spatial gradient operator with respect to the position vector  $\mathbf{q}$ ,  $\chi_n$  is the reconstructed contrast at the  $n$ th iteration of the inversion algorithm, and  $A$  is the area of the imaging domain  $\mathcal{D}$ . The positive parameter  $\delta_n^2$  is chosen to be  $\mathcal{F}^{\mathcal{L}\mathcal{S}}(\chi_n)/\Delta A$ , where  $\Delta A$  is the area of a single cell in the uniformly discretized domain  $\mathcal{D}$ . In the MR-GNI method, the Gauss-Newton optimization is applied to (4); thus, the contrast at the  $(n+1)$ th iteration is updated as  $\chi_{n+1} = \chi_n + \nu_n \Delta\chi_n$ , where  $\Delta\chi_n$  and  $\nu_n$  are the Gauss-Newton correction and an appropriate step-length, respectively. The step-length is obtained via an appropriate line-search method based on that described in [7].

As opposed to the problem considered in [7], the unknown contrast function is complex, and special care must be taken in minimizing (4). Herein, we minimize the cost-functional  $\mathcal{F}_{n+1}(\chi)$  with respect to the complex function  $\chi$  and its complex conjugate  $\chi^*$ , taking them to be two independent functions. It is shown in [10] that this procedure is equivalent to minimizing  $\mathcal{F}_{n+1}(\chi)$  over  $\text{Re}(\chi)$  and  $\text{Im}(\chi)$ , the real and imaginary parts of  $\chi$ . Noting that  $\mathcal{F}_{n+1}^{\text{MR}}(\chi_n) = 1$ , the Gauss-Newton correction  $\Delta\chi_n$  can be found by satisfying

$$\left[ \frac{\partial^2 \mathcal{F}^{\mathcal{L}\mathcal{S}}}{\partial\chi^* \partial\chi} \Big|_{\chi=\chi_n} + \mathcal{F}^{\mathcal{L}\mathcal{S}}(\chi_n) \frac{\partial^2 \mathcal{F}_{n+1}^{\text{MR}}}{\partial\chi^* \partial\chi} \Big|_{\chi=\chi_n} \right] (\Delta\chi_n) = -\frac{\partial \mathcal{F}^{\mathcal{L}\mathcal{S}}}{\partial\chi^*} \Big|_{\chi=\chi_n} - \mathcal{F}^{\mathcal{L}\mathcal{S}}(\chi_n) \frac{\partial \mathcal{F}_{n+1}^{\text{MR}}}{\partial\chi^*} \Big|_{\chi=\chi_n}. \quad (6)$$

In the discrete domain, with the contrast function  $\chi$  discretized into a complex vector  $\underline{\chi}$  using pulse basis functions and the measured data stored in a complex vector  $\underline{E}^{\text{meas}}$ , satisfying (6) is equivalent to solving

$$\left( \mathbf{J}_n^H \mathbf{J}_n + \mathcal{F}^{\mathcal{L}\mathcal{S}}(\underline{\chi}_n) \mathcal{L}_n \right) \Delta\underline{\chi}_n = -\mathbf{J}_n^H (\underline{E}_n^{\text{scat}} - \underline{E}_n^{\text{meas}}) - \mathcal{F}^{\mathcal{L}\mathcal{S}}(\underline{\chi}_n) \mathcal{L}_n \underline{\chi}_n \quad (7)$$

where  $\mathbf{J}_n$  is the Jacobian matrix containing the Fréchet derivative of  $E^{\text{scat}}(\mathbf{p}, \underline{\chi})$  with respect to  $\underline{\chi}$  evaluated at  $\underline{\chi}_n$  [11], and  $\underline{E}_n^{\text{scat}}$  is the complex vector containing the simulated scattered field at the observation points corresponding to the predicted contrast  $\underline{\chi}_n$ . The regularization operator  $\mathcal{L}_n$  is the discrete form of the operator  $-\nabla \cdot (b_n \nabla)$ , where  $b_n^{-1} = A(|\nabla\chi_n(\mathbf{q})|^2 + \delta_n^2)$  [7].

As can be seen in (7), the weight of the regularization operator, determined by  $\mathcal{F}^{\mathcal{L}\mathcal{S}}(\underline{\chi}_n)$ , changes automatically throughout the iterations. That is, as the inversion algorithm gets closer to the true contrast via minimizing the discrepancy between the measured and simulated data, the regularization

weight is lessened, thus providing an adaptive regularization [12].

The regularization operator,  $\mathcal{L}_n$ , is capable of providing an edge-preserving regularization as defined in [13]. This can be explained as follows. Assuming that one specific region of  $\chi_n$  is homogeneous, the weight  $b_n$  will be almost constant for that part, and the regularization operator  $\mathcal{L}_n$ , when applied to that region, will be approximately  $-b_n \nabla^2$ . The Laplacian operator favors smooth solution, and therefore, the smoothness will be preserved in that region. On the other hand, if there is a large gradient in  $\chi_n$  (e.g., an edge in the image) in some part of the imaging domain, the corresponding  $b_n$  for that region will be small. Thus, the steep gradient will not be smoothed out, but will be preserved [13].

In our implementation, we have used a five-point stencil to calculate the gradient part of  $\mathcal{L}_n$ . The inversion algorithm terminates if one of the following four empirically chosen conditions is satisfied: 1) the data misfit  $\mathcal{F}^{\mathcal{L}\mathcal{S}}(\chi)$  is less than a prescribed error (set to  $10^{-3}$ ); 2) the difference between two successive data misfits becomes less than a prescribed value (set to  $10^{-4}$ ); 3) the difference between two successive reconstructed contrasts becomes less than a prescribed value (set to  $10^{-5}$ ); or 4) the total number of iterations exceeds a prescribed maximum (set to 50). From our experience with the MR-GNI method, the first three termination criteria are very important as the MR-GNI method may distort the reconstructed contrast if it proceeds after reaching the noise level of the measured data or after converging to a contrast.

### III. EXPERIMENTAL RESULT

We first show that the MR-GNI algorithm is capable of inverting the experimental data collected by the UPC Barcelona group [9]. These data sets were collected using a near-field 2.33-GHz microwave scanner system that consists of 64 water-immersed antennas equispaced on a 12.5-cm-radius circular array [9]. In their system, for each case of using one of the 64 antennas as a sole transmitter, field data is collected using only the 33 antennas positioned in front of the transmitting antenna. The measured data is then calibrated such that a line source perpendicular to the imaging domain can be used to model the incident field inside  $\mathcal{D}$  (2D-TM assumption). The data collection tank is filled with a background solution of water, with the relative permittivity  $\epsilon_b = 77.3 + j8.66$  at 2.33 GHz. Herein, we invert the data collected from a human forearm (data file: BRAGREG.ASC). The inversion results are constrained to lie within the region defined by  $0 \leq \text{Re}(\epsilon_r) \leq 80$  and  $0 \leq \text{Im}(\epsilon_r) \leq 20$ , as in [5].

We consider the imaging domain  $\mathcal{D}$  to be a  $0.094 \text{ m} \times 0.094 \text{ m}$  square discretized into  $60 \times 60$  pulse basis functions and start the MR-GNI algorithm with  $\chi = 0$ . The reconstruction of this target after 13 iterations is shown in Fig. 1(a) and (b). The overall structure of the forearm can be seen in the images of the real and imaginary parts of the complex permittivity. The MR-GNI inversion is very similar to the MR-CSI reconstruction of this target [5]. The expected relative permittivities are approximately  $54 + j11$  for muscle and  $12 + j2.5$  for bones at  $f = 2.33 \text{ GHz}$ , according to [14]. Similar to MR-CSI reconstruction of this target [5], the expected complex permittivity of the muscle is reconstructed well. However, the reconstructed real and imaginary parts of the bone complex permittivity

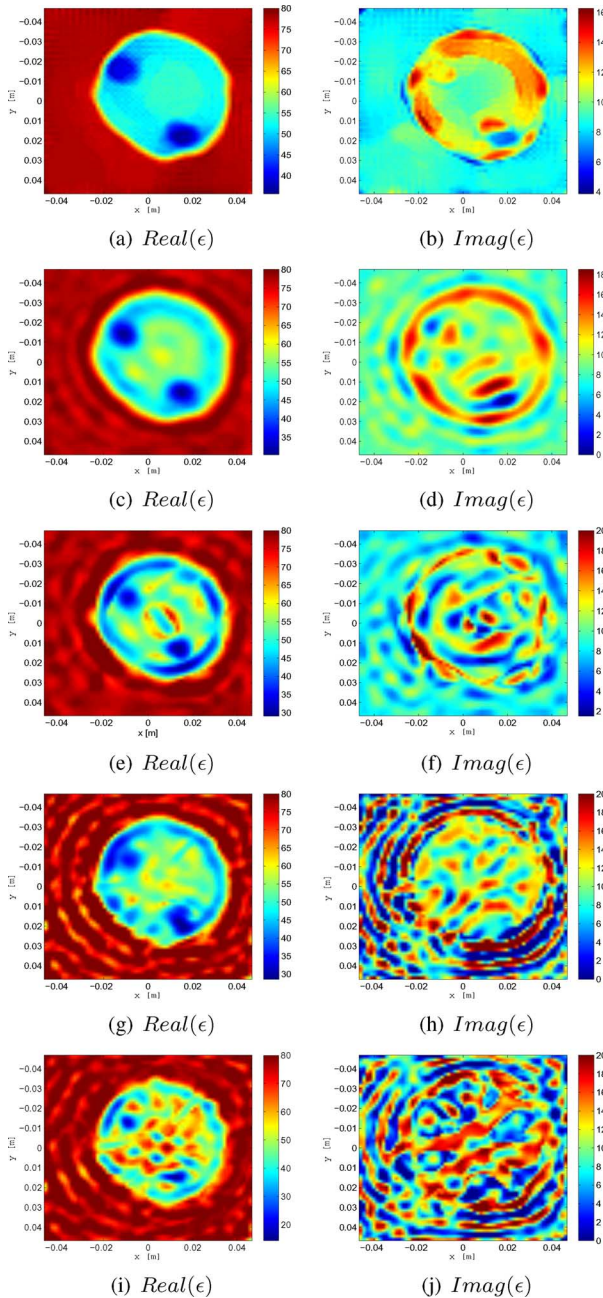


Fig. 1. Reconstructed relative complex permittivity of a real human forearm (BRAGREG data set) using (a), (b) MR-GNI; (c), (d) GNI with the additive-multiplicative  $L_2$ -norm regularizer; (e), (f) GNI with the additive  $L_2$ -norm regularizer; (g), (h) GNI with identity Tikhonov regularizer; and (i), (j) GNI with Krylov subspace regularization.

are higher than their expected values due to the low dynamic range of the collected data [3], [5] as well as the use of the 2D-TM approximation for what is really a three-dimensional (3D) problem. It should be noted that the contribution to the measured scattered field arising from within the bones is very small due to the high reflection coefficient at the bone-muscle boundary. Considering the low dynamic range of the system, information arising from scattering within the bones may be buried in the noise, resulting in an underestimated *contrast* for the bones—i.e.,  $-0.54 + j0.013$ , as opposed to the expected value  $-0.84 + j0.015$ .

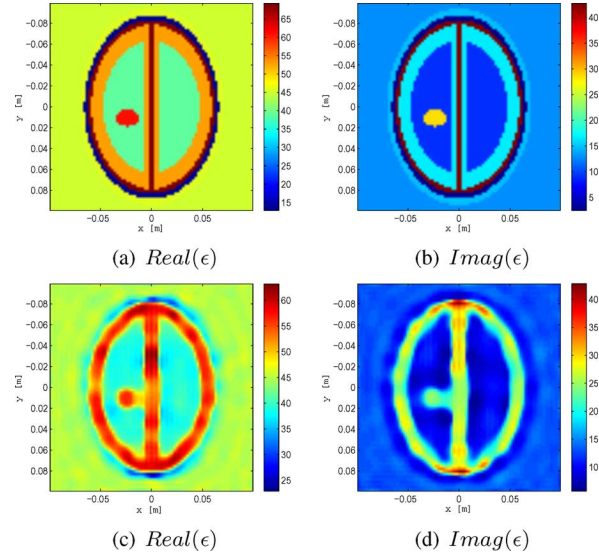


Fig. 2. Brain test case: (a), (b) true model; (c), (d) reconstructed permittivity.

The reconstruction of this target using GNI in conjunction with some other regularization techniques—namely, additive-multiplicative  $L_2$ -norm [11], additive  $L_2$ -norm [15], identity Tikhonov [4], and Krylov subspace [1] regularizers—is shown in Fig. 1(c)–(j). Comparing the GNI reconstructions of this target using different regularization methods, the edge-preserving characteristic of the utilized MR can clearly be seen.

#### IV. SYNTHETIC DATA RESULTS

In this section, we show the performance of the MR-GNI algorithm against synthetically derived data for simplified brain and realistic breast models. In both cases, the data is generated on a grid that is different than the one used in the inversion algorithm. Also, 3% noise was added to the collected scattered field on the measurement domain according to the relation given in [16]. In these two cases, we start the MR-GNI algorithm with the initial guess  $\chi = 0$ .

##### A. Brain Model

The 2D brain model is based on the model presented in [2] and [6], which consists of a layer of skin followed by bone, cerebral spinal fluid (CSF), gray matter, white matter, and an area of stroke; see Fig. 2(a) and (b). The frequency of operation is chosen to be 1 GHz. The relative complex permittivities of the different parts of the model are taken from [14] and are given as  $\epsilon_{r,\text{skin}} = 46 + j15$ ,  $\epsilon_{r,\text{bone}} = 12.8 + j2.4$ ,  $\epsilon_{r,\text{CSF}} = 69.3 + j42.8$ ,  $\epsilon_{r,\text{gray}} = 52.8 + j16.9$ ,  $\epsilon_{r,\text{white}} = 38.6 + j9.0$ , and  $\epsilon_{r,\text{stroke(blood)}} = 61.1 + j28.5$ . The relative permittivity of the background medium is chosen to be  $\epsilon_b = 45 + j13$ . The synthetic scattering data, which includes 32 transmitters with 32 receivers per transmitter, is generated on a grid of  $100 \times 100$  square pulses in a  $0.22 \text{ m} \times 0.22 \text{ m}$  square. Both transmitters and receivers are located on a circle of radius 0.15 m. The imaging domain is chosen to be a  $0.2 \text{ m} \times 0.2 \text{ m}$  square that is discretized into  $79 \times 79$  square pulses. The reconstruction of this model is shown in Fig. 2(c) and (d), where the stroke region is clearly visible. Although the bone and CSF region is not reconstructed,

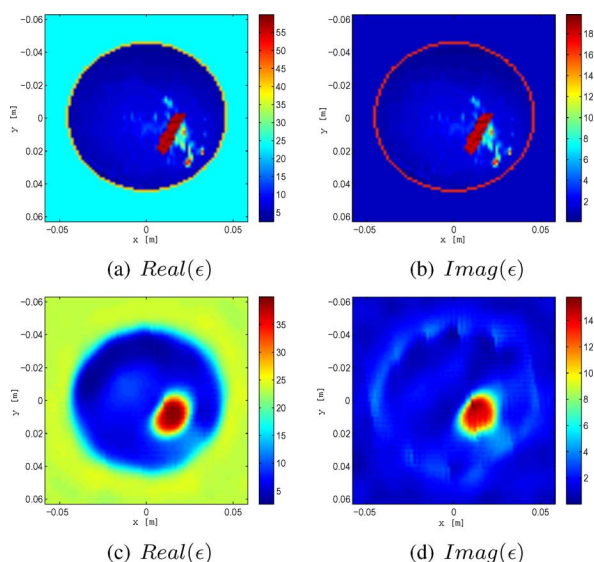


Fig. 3. Breast test case: (a), (b) true model; (c), (d) reconstructed permittivity.

the reconstructed permittivities of the white matter, gray matter, and stroke are close to the expected values.

### B. Breast Model

The 2D breast model is taken from the University of Wisconsin-Madison breast model repository, which provides anatomically realistic MRI-derived 3D breast models [17]. The complex permittivities of different tissues in these models are based on the studies reported in [18]. The utilized breast model, shown in Fig. 3(a) and (b), is a 2D slice of the *scattered fibroglandular* model to which an elliptically-shaped tumor was added. The complex permittivity of the tumor region was taken from the 75th percentile group given in [18]. The frequency of operation is chosen to be 1 GHz, at which the complex permittivity of the background medium is  $23.4 + j1.13$ . The breast model is illuminated by 32 transmitters, and the simulated scattered data is collected using 32 receivers per transmitter. The simulated data is generated on a grid of  $95 \times 100$  square pulses in a  $0.13 \text{ m} \times 0.14 \text{ m}$  rectangle. The receivers and transmitters are located on a circle of radius 0.1 m. The imaging domain is a  $0.12 \text{ m} \times 0.13 \text{ m}$  rectangle that is discretized into  $77 \times 83$  pulses. The inversion result is shown in Fig. 3(c) and (d), where the overall structure of the breast can be easily seen. Although the complex permittivity of fatty tissues has been reconstructed well, the complex permittivity of the tumor has been underestimated. This is probably due to the fact that the algorithm has averaged out the permittivities of transitional tissues and the tumor region as it was unable to resolve these two regions at the selected frequency.

## V. CONCLUSION

In all the cases considered herein, the MR-GNI method has provided meaningful reconstructions of experimental and synthetic biomedical data. The main advantage of the MR-GNI method, compared to other forms of Gauss–Newton inversion, is

that the MR-GNI algorithm automatically provides an adaptive regularization, and the user does not need to choose a regularization parameter for the inversion algorithm. It also provides an edge-preserving regularization through its use of the weighted  $L_2$ -norm total variation MR.

## REFERENCES

- [1] T. Rubæk, P. M. Meaney, P. Meincke, and K. D. Paulsen, "Nonlinear microwave imaging for breast-cancer screening using Gauss–Newton's method and the CGLS inversion algorithm," *IEEE Trans. Antennas Propag.*, vol. 55, no. 8, pp. 2320–2331, Aug. 2007.
- [2] S. Y. Semenov and D. R. Corfield, "Microwave tomography for brain imaging: Feasibility assessment for stroke detection," *Int. J. Antennas Propag.*, pp. 1–8, 2008.
- [3] J. Mallorqui, N. Joachimowicz, A. Broquetas, and J. C. Boloiney, "Quantitative images of large biological bodies in microwave tomography by using numerical and real data," *Electron. Lett.*, vol. 32, no. 23, pp. 2138–2140, Nov. 1996.
- [4] N. Joachimowicz, J. J. Mallorqui, J. C. Bolomey, and A. Broquetas, "Convergence and stability assessment of Newton-Kantorovich reconstruction algorithms for microwave tomography," *IEEE Trans. Med. Imag.*, vol. 17, no. 4, pp. 562–569, Aug. 1998.
- [5] A. Abubakar, P. M. van den Berg, and J. J. Mallorqui, "Imaging of biomedical data using a multiplicative regularized contrast source inversion method," *IEEE Trans. Microw. Theory Tech.*, vol. 50, no. 7, pp. 1761–1777, Jul. 2002.
- [6] C. Gilmore, A. Abubakar, W. Hu, T. Habashy, and P. van den Berg, "Microwave biomedical data inversion using the finite-difference contrast source inversion method," *IEEE Trans. Antennas Propag.*, vol. 57, no. 5, pp. 1528–1538, May 2009.
- [7] A. Abubakar, T. M. Habashy, V. L. Druskin, L. Knizhnerman, and D. Alumbaugh, "2.5D forward and inverse modeling for interpreting low-frequency electromagnetic measurements," *Geophysics*, vol. 73, no. 4, pp. F165–F177, Jul.–Aug. 2008.
- [8] A. Abubakar *et al.*, "A three-dimensional multiplicative-regularized non-linear inversion algorithm for cross-well electromagnetic and controlled-source electromagnetic applications," *SEG Expanded Abstracts*, vol. 27, pp. 584–588, 2008.
- [9] A. Broquetas, J. Romeu, J. M. Rius, A. R. Elias-Fuste, A. Cardama, and L. Jofre, "Cylindrical geometry: a further step in active microwave tomography," *IEEE Trans. Microw. Theory Tech.*, vol. 39, no. 5, pp. 836–844, May 1991.
- [10] A. van den Bos, "Complex gradient and Hessian," *Proc. Vision, Image Signal Process.*, vol. 141, no. 6, pp. 380–383, 1994.
- [11] J. D. Zaeytijd, A. Franchois, C. Eyraud, and J.-M. Geffrin, "Full-wave three-dimensional microwave imaging with a regularized Gauss–Newton method—Theory and experiment," *IEEE Trans. Antennas Propag.*, vol. 55, no. 11, pp. 3279–3292, Nov. 2007.
- [12] M. S. Zhdanov, *Geophysical Inverse Theory and Regularization*. Amsterdam, The Netherlands: Elsevier, 2002.
- [13] P. Charbonnier, L. Blanc-Féraud, G. Aubert, and M. Barlaud, "Deterministic edge-preserving regularization in computed imaging," *IEEE Trans. Image Process.*, vol. 6, no. 2, pp. 298–311, Feb. 1997.
- [14] C. Gabriel, S. Gabriel, and E. Corthout, "The dielectric properties of biological tissues: III. Parametric models for the dielectric spectrum of tissues," *Phys. Med. Biol.*, vol. 41, no. 11, pp. 2271–2294, Nov. 2000.
- [15] A. E. Bulyshev, A. E. Souvorov, S. Y. Semenov, R. H. Svenson, A. G. Nazarov, Y. E. Sizov, and G. P. Tastis, "Three dimensional microwave tomography. Theory and computer experiments in scalar approximation," *Inverse Problems*, vol. 16, pp. 863–875, 2000.
- [16] A. Abubakar, P. M. van den Berg, and S. Y. Semenov, "A robust iterative method for Born inversion," *IEEE Trans. Geosci. Remote Sens.*, vol. 42, no. 2, pp. 342–354, Feb. 2004.
- [17] E. Zastrow, S. Davis, M. Lazebnik, F. Kelcz, B. Van Veen, and S. Hagness, "Development of anatomically realistic numerical breast phantoms with accurate dielectric properties for modeling microwave interactions with the human breast," *IEEE Trans. Biomed. Eng.*, vol. 55, no. 12, pp. 2792–2800, Dec. 2008.
- [18] M. Lazebnik *et al.*, "A large-scale study of the ultrawideband microwave dielectric properties of normal, benign, and malignant breast tissues obtained from cancer surgeries," *Phys. Med. Biol.*, vol. 52, pp. 6093–6115, 2007.